Recent Advances in InSAR Image Processing and Analysis

3

3.1 Introduction and Background

InSAR is a spaceborne mapping tool capable of remotely sensing small changes in land surface elevation at unprecedented spatial resolution. As discussed in previous chapters, InSAR utilizes two or more coherent phase signals acquired at different times from the same area to map ground deformation that may have occurred during the intervening period. In theory, InSAR measures phase differences between two SAR images that result from the difference in round-trip path length from a radar to the same ground point. The phase difference can be processed to map line-of-sight ground displacement at a horizontal resolution of tens of meters over large areas with sub-centimeter accuracy.

The advent of InSAR has led to significant improvement in documentation and understanding of Earth surface motions. Nonetheless, several error sources in conventional InSAR measurements limit the technique's effectiveness in some cases (see Chap. 1). If the goal is to map ground deformation, these include phase residuals due to inaccuracies in the DEM used to produce a differential interferogram, atmospheric path-delay anomalies, phase ramp caused by orbital errors, phase noise, and phase unwrapping errors. To reduce the effects of such errors, a new technique called multi-temporal InSAR (MTInSAR)—in which a set of InSAR images of the same area acquired on different dates are jointly analyzed together—was proposed in the late 1990s. MTInSAR methods have ushered in a new era of advanced radar remote sensing by reducing or even eliminating error sources that plague conventional InSAR analysis. Current MTInSAR techniques can be divided into three categories. The first involves the generation of a stack of interferograms with respect to a single master image. Examples include persistent scatterer InSAR (PSInSAR) (Ferretti et al. 2000, 2001), Stanford method for PS (StaMPS) (Hooper et al. 2004; Hooper 2008) and spatio-temporal unwrapping network (STUN) (Kampes 2006). In the second category are techniques that make use of multi-master interferograms; examples include the stacking analysis method (Sandwell and Price 1998), the Small BAseline Subset (SBAS) approach (Berardino et al. 2002; Lanari et al. 2004), the coherent pixel technique (CPT) (Blanco et al. 2008; Mora et al. 2003), and temporally coherent point InSAR (TCPInSAR) (Zhang et al. 2011b, 2012). A third (hybrid) category includes techniques that combine single- and multi-master interferogram analysis methods (Hooper et al. 2012).

During the past decade, several algorithms have been developed under the general framework of MTInSAR. Significant advances have been made in four areas: (1) phase-coherent point identification; (2) atmospheric artifact reduction; (3) removal of orbital errors; and (4) handling of phase ambiguity. In this chapter we discuss the essential features of each approach and provide an example of their application to the 2008 eruption at Mount Okmok, Alaska.

3.2 Phase-Coherent Point Identification

As discussed in previous chapters, phase coherence must be maintained in order for useful information to be derived from an interferogram using conventional InSAR techniques. Practically speaking, only image pairs with temporal separations of less than a few years can be used for deformation mapping under ideal conditions (flat, rocky terrain). In sloped or vegetated terrain, the time constraint is even more severe. This generally limits the application of conventional InSAR techniques to rapid-motion phenomena such as volcanic eruptions and earthquakes. Deformation that occurs at lower rates over longer timescales is not amenable to this approach, because coherence is lost before the signal exceeds the detection threshold. In such cases, an alternate strategy is required.

It was recognized in the late 1990s that useful information could be retrieved from isolated radar scatterers that maintain high coherence for long periods of time, such as boulders, tree trunks, and buildings (Hooper et al. 2007). Such persistently coherent scatterers, which might occupy

Z. Lu and D. Dzurisin, *InSAR Imaging of Aleutian Volcanoes*,
Springer Praxis Books, DOI: 10.1007/978-3-642-00348-6_3,

only a few percent of the pixels in an otherwise non-coherent image, are the key to all MTInSAR techniques. Analogous to the role of benchmarks in conventional ground-based surveys, these scatterers that do not change their radar backscattering signatures over time can be used as monuments to track surface displacements at millimeter accuracy (Ferretti et al. 2000, 2001). Such persistent scatterers are pre-existing targets of opportunity that can be used as temporally and spatially coherent reference points; hereafter, this type of feature will be referred to as a "persistent scatterer" (PS). Because PSs have large scattering cross sections relative to their physical size and their physical size is small compared to a SAR resolution element, PSs can be treated as point targets. The SAR backscattering signal of a PS has a broadband spectrum, which means that the phase of a PS pixel correlates over much longer time intervals and over much larger baseline separations than other types of pixels. Therefore, the problem posed by decorrelation in conventional InSAR can be overcome for pixels that contain one or more PSs. Targets that do not possess the characteristics of PSs are called distributed scatterers (DSs). Unlike point-wise PSs whose coherence is insensitive to spatial or temporal baselines, DSs can maintain high phase quality only in interferograms with limited spatial and temporal baselines. Nonetheless, they are useful for multi-master MTInSAR processing. In the following sections we review several approaches used to identify phase-coherent points, both for single-master MTInSAR (Sects. 3.2.1–3.2.6) and for multi-master MTInSAR (Sects. 3.2.7–3.2.8).

3.2.1 Amplitude Dispersion Index

The amplitude dispersion index (ADI) was first introduced by Ferretti et al. (2000, 2001) in their PSInSAR technique, which employs a stack of single-master interferograms without considering baseline limitations. Because interferograms can be greatly affected by spatial decorrelation, it is difficult to use a spatially estimated coherence criterion to select pixels with high phase quality in interferograms with extremely long baselines. Distributed targets in SAR images exhibit typical SAR speckle behavior, i.e., the backscattering intensity of a single-look image has a large variability around the ensemble average. Speckle is a source of spatial and temporal variability in backscatter intensity. PSs by definition do not exhibit this speckle behavior. Consequently, if a large number of SAR images with different temporal and spatial baselines are considered, low temporal variability in backscattering intensity is an indicator of the presence of point targets (PSs). Ferretti et al. (2000, 2001) coined the term amplitude dispersion index (D_A) for this indicator, i.e., the ratio between the standard deviation (σ_A) and the mean value of multi-temporal backscattering intensity (m_A):

$$D_A = \frac{\sigma_A}{m_A} \tag{3.1}$$

Simulation tests indicate that the amplitude dispersion index is a satisfactory approximation for phase dispersion of pixels with high signal-to-noise ratio (SNR) (Ferretti et al. 2001). For this approach to work, radiometric calibration and image co-registration with adequate interpolation are important.

3.2.2 Signal-to-Clutter Ratio

The signal-to-clutter ratio (SCR) approach was first suggested by Adam et al. (2004) to identify coherent points for their PSInSAR processor. Assuming that a PS pixel returns a deterministic signal that is contaminated by random circular Gaussian distributed clutter, the SCR can be estimated by computing the ratio of the power of a PS candidate pixel to that of its neighbors. The relationship between the SCR and the phase standard variance (σ_ϕ) can be defined as:

$$\sigma_\phi = \frac{1}{\sqrt{2 \cdot SCR}}, \; SCR = \frac{s^2}{c^2} \tag{3.2}$$

where s represents the amplitude of the dominant scatterer and c the clutter in the surroundings (i.e., distributed targets). A pixel with a high SCR at each acquisition is often selected as a PS candidate. Equation 3.2 can be used to determine a reasonable threshold of SCR. For example, if a phase standard variance of 0.5 rad^2 is desired, the minimum acceptable SCR value is 2. Adam et al. (2004) showed that SCR and D_A are based on the same signal model for a dominant point scatterer surrounded by incoherent background clutter, and the two quantities are related by the expression:

$$D_A = \frac{1}{\sqrt{2 \cdot SCR}} \tag{3.3}$$

SCR estimation can be performed with a single SAR image, whereas D_A estimation requires multiple interferograms. Therefore the SCR approach is less demanding on the number of SAR images required.

3.2.3 Spectral Diversity

When processing a single scene of SAR data into an image with different looks and different fractional range and/or azimuth bandwidths, only point targets maintain nearly the same backscattering intensity. Pixels with low variability in

backscattering intensity are identified as PS candidates. Including more scenes excludes non-stationary PSs (Werner et al. 2003).

3.2.4 Phase Stability

In order to identify a sufficient number of coherent points in non-urban areas, where scatterers usually have low SNR, Hooper et al. (2004) proposed a PS selection method based on the phase stability of targets. Phase stability is analyzed under the assumption that deformation is spatially correlated. The phase values of neighboring PS candidates are averaged, and those with lowest residual noise (variability) are selected. Given a set of topographically corrected interferograms, a measure of phase stability can be defined as

$$\gamma_x = \frac{1}{N}\left|\sum \exp\{j(\Phi_{\text{int},\,x,\,i} - \bar{\Phi}_{\text{int},\,x,\,i} - \Delta\hat{\Phi}_{\varepsilon,\,x,\,i})\}\right| \quad (3.4)$$

where N is the number of interferograms, $\Phi_{\text{int},\,x,\,i}$ is the differential phase of the xth interferogram, $\bar{\Phi}_{\text{int},\,x,\,i}$ is the mean phase of all PS candidates within a circular patch centered on pixel x with radius L, and $\Delta\hat{\Phi}_{\varepsilon,\,x,\,i}$ is the estimated phase component contributed by DEM errors. To calculate the mean phase of patches efficiently, PS candidates selected using the ADI method with a high threshold value (Ferretti et al. 2000, 2001) are taken as initial selections. The threshold value of γ_x is selected in a probabilistic fashion assuming that coherence values less than 0.3 correspond to noisy non-PS pixels.

3.2.5 Maximum Likelihood Estimation

Shanker and Zebker (2007) proposed an alternative PS selection method based on the maximum likelihood estimation algorithm. In this case the noise term, ϕ_n, is related to the signal-to-noise ratio, γ, by the following function:

$$P(\phi_n) = \frac{1-|\rho|^2}{2\pi}\cdot\frac{1}{1-(|\rho|\cos\phi_n)^2} \cdot\left\{1+\frac{|\rho|\cos\phi_n\cdot\arccos(-|\rho|\cos\phi_n)}{\sqrt{1-(|\rho|\cos\phi_n)^2}}\right\} \quad (3.5)$$

and $|\rho| = \frac{1}{1+\gamma^{-1}}$.

Given a series of N interferograms, the value of γ can be estimated by maximizing $P(\gamma|\phi_{n_1},\ldots,\phi_{n_N})$, which is the conditional probability of γ for $\phi_{n_1},\ldots,\phi_{n_N}$. According to Bayes' rule,

$$P(\gamma|\phi_{n_1},\ldots,\phi_{n_N}) = \frac{P(\phi_{n_1},\ldots,\phi_{n_N}|\gamma)\cdot P(\gamma)}{P(\phi_{n_1},\ldots,\phi_{n_N})} \quad (3.6)$$

Since $P(\phi_{n_1},\ldots,\phi_{n_N})$ is independent of γ and assuming $P(\gamma)$ is constant for all γ, Eq. 3.6 can be restated as maximizing the product:

$$P(\phi_{n_1}|\gamma)\cdot P(\phi_{n_2}|\gamma)\cdot\cdots\cdot P(\phi_{n_N}|\gamma), \qquad \forall\gamma \quad (3.7)$$

The derived maximum likelihood estimation γ is compared to a pre-determined threshold, $\gamma_{threshold}$, which is set by experience. In this way, candidate PS pixels with maximum likelihood estimations that exceed the threshold are accepted as valid .

3.2.6 Integration of Distributed Scatterer and Persistent Scatterer Techniques

To improve the spatial coverage of deformation estimates in non-urban areas, Ferretti et al. (2011) proposed to jointly analyze persistent scatterers (PS) and distributed scatterers (DS). In contrast to PSs that are associated with manmade structures, boulders, and outcrops, DSs correspond to debris areas, non-cultivated land with short vegetation, or desert areas. A spatially adaptive de-speckle filter is first applied to identity DSs, which are defined as statistically homogenous pixels. Because phase values of PSs are generally deterministic and the phases of DSs are stochastic, a phase triangulation algorithm is applied to estimate optimum phase values for DSs based on candidate pixels' coherence properties and statistical characteristics. Then DSs and PSs can be combined and processed using standard PSInSAR techniques to produce time-series deformation measurements (Ferretti et al. 2011).

3.2.7 Coherence Map

The aforementioned methods are designed to identify persistent scatterers or distributed scatterers from single-master interferogram stacks, for which there is no limitation on the length of spatial or temporal baselines. For interferograms with moderate-length spatial and temporal baselines, in addition to PSs there often are many DSs that produce high quality phase signals. Without a doubt, the spatial resolution of an InSAR-derived deformation map can be improved significantly by including both PSs and DSs with high phase quality. The coherence map method has been used to select coherent pixels from interferograms with relatively short baselines. After eliminating the phase components related to topography and flat Earth, the coherence value of each pixel ($|\hat{\gamma}_i|$) in selected interferograms can be estimated. A mean coherence map then can be generated using the relationship:

$$\gamma_{mean} = \frac{1}{N}\sum_{i=0}^{N-1} |\hat{\gamma}_i| \tag{3.8}$$

where N is the number of interferograms. All pixels with a mean coherence greater than some selection threshold are accepted as coherent point candidates. Mora et al. (2003) suggested a minimum value of mean coherence of 0.25 for coherence maps estimated using a 4 × 16 or a 5 × 20 pixel window (range x azimuth) with C-band ERS-1/2 and Envisat/ASAR data.

3.2.8 Offset Deviation

One challenge faced by all of the current coherent point selection methods is that the choices of threshold values and patch sizes depend heavily on an individual's experience. It is difficult to know a priori the optimal values to balance the phase quality and spatial density of points deemed to be coherent. Zhang et al. (2011a) proposed an alternative method for coherent point selection. The method is based mainly on the standard deviation of the estimated coregistration offsets derived by Bamler (2000), and it makes use of the fact that the offsets estimated from strong scatterers are less sensitive to the window size and oversampling factor used than those from distributed scatterers. The method can be applied when at least two SAR images are available for a given target. For each image pair, after initial coregistration an offset vector at each pixel (OT_j) is generated by changing the window size (e.g., from 4 × 4 to 32 × 32 with a step of 4 or 8):

$$OT_j = [\, ot_{j1} \quad ot_{j2} \quad \cdots \quad ot_{jN} \,] \tag{3.9}$$

where ot_{ji}, $i = 1, 2, \cdots N$ is the offset estimated with a given window size at the jth pixel. Pixels whose offset standard deviations are smaller than the expected coregistration precision (e.g., 0.1 pixel) are selected as coherent points.

3.3 Atmospheric Artifact Reduction

Current satellite-based SAR systems orbit the Earth at altitudes of 500–800 km. The electromagnetic waves transmitted by these systems must propagate through the atmosphere twice and are subject to small variations in the index of refraction along the lines of propagation. Differences in atmospheric temperature, pressure, and water vapor content at two observation times cause changes in the atmospheric path delay and consequent errors in interferograms (e.g., Zebker et al. 1997). Such path-delay errors can reduce the accuracy of interferometrically derived crustal deformation measurements from several millimeters under ideal (time-invariant) conditions to 2–3 cm under more typical conditions. Atmospheric artifacts can be characterized as spatially correlated and temporally random signals—a key characteristic that provides a basis for developing methods to mitigate their effects.

3.3.1 Differencing Operation Among Neighboring Pixels

In topography-removed interferograms, pixel values (phases) that are affected by atmospheric path delays are spatially correlated at dimensions ranging from several meters to several tens of kilometers (i.e., the typical scale of atmospheric inhomogeneities). Therefore, differencing neighboring pixels could in theory reduce the effect of path delays by removing common-mode errors from interferograms. Atmospheric variances as a result of path delays are commonly less than 0.1 rad^2 for points separated by less than 1 km (Williams et al. 1998). However, the effectiveness of spatial differencing depends on the density of coherent points, the arc length (i.e., the length of point pairs), and the correlation dimension of the atmosphere. In current practice, phase differences at two neighboring pixels serve as basic observations in most MTInSAR techniques (e.g., PSI, STUN and StaMPS and TCPInSAR).

3.3.2 Spatial-Temporal Filtering

Spatial-temporal filtering is the most popular method for reducing atmospheric artifacts. It is widely used in almost all MTInSAR techniques. After the effects of the residual elevation with respect to the reference DEM and the mean deformation rate are removed (see Sect. 3.5.1), a spatial-temporal analysis of the phase residuals is carried out to estimate the atmospheric delay component (Ferretti et al. 2000, 2001; Berardino et al. 2001, 2002; Mora et al. 2003; Blanco et al. 2008). For each PS, temporal smoothing based on a triangular filter is performed and the low-pass component is removed. The resulting phase residuals then are spatially filtered using a moving average technique to remove the high frequency component. The results represent the phase difference due to differences in atmospheric conditions at different epochs. If all interferograms are constructed with respect to a single master scene, averaging

the phase component due to atmospheric contamination for all interferograms then can be used to construct the atmospheric contribution due to the master image and each of the other images. However, selecting the optimal window length for the filter (i.e., the triangular window length for the temporal filter and/or the averaging window length for the spatial filter) is not an easy task. Retrieval of the atmospheric delay signal can be compromised, in particular, if the spatial density of PSs and the temporal resolution of SAR images are low.

3.3.3 Topography Correlated Atmosphere Suppression

3.3.3.1 Multi-scale Method

Topography can play a role in producing atmospheric artifacts by inducing differences in temperature, humidity, pressure, and water vapor content in the atmosphere between the acquisition times of two SAR images. The resulting phase structure is treated as a time-variable vertically stratified component of the total atmospheric distortion (Hanssen 2001; Liu 2012). In most cases, a simple linear model is applied to suppress vertically stratified atmospheric delays in unwrapped interferograms:

$$\Delta\phi = k \cdot h + b \tag{3.10}$$

where k and b are the linear and constant terms respectively for the function that relates the phase change $\Delta\phi$ in a topography-removed interferogram and the topography h. The effectiveness of this method is reduced in some cases by the confounding effects of tectonic or other types of ground motion, turbulent atmosphere, inaccurate satellite orbit, etc.

An improved method, proposed by Lin et al. (2010), was developed to overcome the aforementioned drawback by using a multi-scale algorithm. This method explicitly recognizes that different confounding effects are likely to occur at different length scales. In the multi-scale method, a series of Gaussian filters with different spatial scales are used to generate a series of band-passed images for both the topography image and the unwrapped interferogram. A robust linear relationship between the topography and the interferogram phase is given by:

$$\Delta\phi(\lambda_i) = k_{ifm} \cdot h(\lambda_i) + b_{ifm} \tag{3.11}$$

where $\Delta\phi(\lambda_i)$ and $h(\lambda_i)$ are the ith band-passed components of the InSAR phase $\Delta\phi$ and topography h, respectively, and k_{ifm} and b_{ifm} are the linear and constant terms of the function for each interferogram.

When multiple interferograms are available for a study area, an internally consistent transfer function can be estimated for a given time interval by defining a unique set of component time intervals, Δt, for the group of unwrapped interferograms. A linear system is constructed as follows:

$$\begin{bmatrix} h_1(\lambda_1) & h_1(\lambda_1) & 0 & \cdots & 0 & 1 & 1 & 0 & \cdots & 0 \\ h_2(\lambda_2) & h_2(\lambda_2) & 0 & \cdots & 0 & 1 & 1 & 0 & \cdots & 0 \\ & & \vdots & & & & & \vdots & & \\ h_n(\lambda_n) & h_n(\lambda_n) & 0 & \cdots & 0 & 1 & 1 & 0 & \cdots & 0 \\ & & \vdots & & & & & \vdots & & \\ 0 & 0 & h_m(\lambda_m) & \cdots & h_m(\lambda_m) & 0 & 0 & 1 & \cdots & 1 \end{bmatrix} \begin{bmatrix} k_{\Delta t_1} \\ k_2 \\ \vdots \\ k_{\Delta t_p} \\ b_{\Delta t_1} \\ b_{\Delta t_2} \\ \vdots \\ b_{\Delta t_p} \end{bmatrix} = \begin{bmatrix} \Delta\phi_1(\lambda_1) \\ \Delta\phi_1(\lambda_2) \\ \vdots \\ \Delta\phi_1(\lambda_n) \\ \vdots \\ \Delta\phi_m(\lambda_n) \end{bmatrix} \tag{3.12}$$

where $\Delta\phi_m(\lambda_n)$ and $h_m(\lambda_n)$ represent the nth decomposed band of the mth interferogram and the nth decomposed band of the topography, respectively, and $k_{\Delta t_p}$ and $b_{\Delta t_p}$ represent the linear and constant terms for the pth Δt. An L1-norm regression is preferred to solve the linear system in order to suppress outliers (e.g., the unwrapping errors). Note that the entire series of $k_{\Delta t}$ can be recombined to reduce vertically stratified atmospheric delays in any interferometric pair.

3.3.3.2 Wavelet Based Method

Although the multi-scale method has proven in many cases to be effective for removing vertically stratified atmospheric delays, the assumed linear correlation between topography and phase change is not well established in theory. Shirzaei and Bürgmann (2012) proposed a novel method to correct for vertically stratified atmospheric delays without the assumption of a linear model. The basic principle behind the method is multiresolution wavelet analysis, which includes three crucial steps. First, the unwrapped interferogram $U(\zeta, \eta)$ and topography $D(\zeta, \eta)$ are decomposed into

their building blocks on the basis of their frequency properties using the forward wavelet transform:

$$\begin{aligned} U(\zeta,\eta) &= \sum_{i_x}^{p-1}\sum_{i_y}^{q-1} {}^{u}v_{i_x i_y}\Phi_{Ji_x i_y}(\zeta,\eta) \\ &\quad + \sum_{j'}^{J-1}\sum_{i_x}^{p-1}\sum_{i_y}^{q-1}\sum_{\varepsilon}^{3} {}^{u}w^{\varepsilon}_{j' i_x i_y}\Psi^{\varepsilon}_{j' i_x i_y}(\zeta,\eta) \\ D(\zeta,\eta) &= \sum_{i_x}^{p-1}\sum_{i_y}^{q-1} {}^{d}v_{i_x i_y}\Phi_{Ji_x i_y}(\zeta,\eta) \\ &\quad + \sum_{j'}^{J-1}\sum_{i_x}^{p-1}\sum_{i_y}^{q-1}\sum_{\varepsilon}^{3} {}^{d}w^{\varepsilon}_{j' i_x i_y}\Psi^{\varepsilon}_{j' i_x i_y}(\zeta,\eta) \end{aligned} \tag{3.13}$$

where Φ and Ψ are the smoothing and the mother wavelet functions, respectively, with v and w being the associated smoothing and wavelet coefficients. J is the number of wavelet scales, and p, q are the dimensions of the images.

Next, a cross-correlation analysis is applied to determine the correlated coefficients that represent the effects of path delay differences in a vertically stratified atmosphere. This is expected because the wavelet coefficients of two correlated signals are similar over a range of spatial scales. A cross-correlation matrix is calculated to evaluate the similarity between the wavelet coefficients for the wavelet scale j':

$$C^{\varepsilon}_{j'} = {}^{u}w^{\varepsilon}_{j'} \circ {}^{d}w^{\varepsilon}_{j'} \tag{3.14}$$

where $\circ$ represents the operator of the matrix correlation. By applying the down-weighting approach, the down-weighted wavelet coefficients of the unwrapped interferogram can be determined by:

$${}^{u}\widetilde{w}^{\varepsilon}_{j'} = \left(1 - C^{\varepsilon}_{j'}\right) {}^{u}w^{\varepsilon}_{j'} \tag{3.15}$$

Finally, the unwrapped interferogram is corrected by applying a wavelet backward transform with the down-weighted correlated coefficients in the wavelet function. Similar to the multi-scale method, the wavelet method is relatively insensitive to confounding effects such as ground motion or orbital ramp resulting from orbit errors. In practice, the discrete wavelet transform is preferred for the very efficient algorithm in the forward and backward transforms. The number of scales used in the wavelet decomposition can range from 1 to 10, which results in an effective window size between 80 m and 80 km.

3.4 Orbit Error Correction

Orbit errors, characterized typically as long-wavelength artifacts, commonly exist in InSAR images as a result of inaccurate determination of the sensor state vector. In the conventional InSAR approach, the orbital contribution is usually removed from an unwrapped interferogram by fitting a low-order polynomial to the long-wavelength signal. The coefficients of the polynomial are determined either by ground control points (GCPs) or under the assumption that no deformation occurred in some part of the interferogram. Obviously, the degree to which the polynomial can remove the effect of orbit errors depends largely on the precision of GCPs or the validity of the no-deformation assumption. Moreover it is difficult (or impossible) to separate any real long-wavelength deformation signal from the effect of orbit errors by applying a best-fitting polynomial to individual interferograms. Generally speaking the phase component due to orbit errors appears in an interferogram as a smoothly varying pattern. Long-wavelength orbital artifacts are obvious in some cases, but in other cases they can be obscured by other phase components. An important difference between orbital artifacts and long-wavelength deformation signals is that the former are characterized by relatively weak temporal correlation. Recent advances in orbit error removal take advantage of this fact by making full use of the spatial-temporal characteristics of orbit errors.

3.4.1 Network Approach

Instead of focusing on a single image pair, Biggs et al. (2007) proposed a network method to identify and remove orbital artifacts using constraints from a stack of interferograms. The core idea behind the method is that the orbit errors in each interferogram can be treated as a contribution from each SAR acquisition. This is a reasonable assumption because interferograms are a linear combination of SAR images. Under the assumptions that: (1) unwrapped phases in an interferogram are mainly contributed by orbit errors that have a planar form, and (2) any other contribution can be treated as noise, for pixel, p, at location (x_p, y_p), the interferometric phase ($\phi_{m,n,p}$) can be expressed as a linear function of two parameters, u and v, for each of two image acquisitions, m and n, and the noise term, $w_{m,n}$:

$$\phi_{m,n,p} = u_m x_p - u_n x_p + v_m y_p - v_n y_p + w_{mn}. \tag{3.16}$$

For each pixel in each interferogram, a similar equation can be written. Thus a large sparse linear equation system is generated, which shows the relationship between the unwrapped phases and coefficients of polynomials associated with each SAR acquisition. Because the system is intrinsically underdetermined, truncated singular value decomposition is used to find the minimum norm solution (Biggs et al. 2007). Once the orbital parameters are estimated, they can be used to construct and remove the orbit-error contribution for each interferogram.

3.4.2 Joint Model

Following Biggs et al. (2007), Zhang (2013) proposed a novel approach that can jointly estimate orbital errors together with deformation parameters and DEM errors. In this method, the assumption that an interferogram is dominated by orbital errors is no longer necessary. Moreover, the approach is capable of separating long-wavelength deformation from the effect of orbit errors. The basic observation of the joint model approach is the differential phase at the arcs (coherent point pairs) which can reduce the effects of spatially correlated atmospheric artifacts. Considering M differential interferograms generated from N SAR images and G arcs constructed from P coherent points, the observations for all the interferograms can be denoted by:

$$\begin{aligned} \underset{(M)\times 1}{\Delta\Phi} &= \left[\Delta\Phi^1 \Delta\Phi^2 \cdots \Delta\Phi^M\right]^T \\ \Delta\Phi^i &= \left[\Delta\phi_1^i \Delta\phi_2^i \cdots \Delta\phi_G^i\right]^T, i = 1 \cdots M \end{aligned} \tag{3.17}$$

where $\Delta\phi_j^i, j = 1 \cdots G$ is the phase difference at a given arc. To avoid an underdetermined system, a reference image is chosen arbitrarily and assumed to be free of orbital error. The following polynomial is used to represent the relative orbital error of a pixel P in the jth acquisition at coordinate (X, Y) with respect to the reference image:

$$\phi_{orb,\,slc,\,p}^j = a^j X + b^j Y + c^j XY,\ j = 1 \cdots N-1 \tag{3.18}$$

where a^j, b^j and c^j are the unknown coefficients to be estimated. The phase components ($\Delta\Phi_{\mathbf{orb}}$) due to orbit errors at all of the arcs in the interferograms can be obtained as follows:

$$\underset{(M\times G)\times 1}{\Delta\Phi_{\mathbf{orb}}} = \underset{((N-1)\times 3)\times 1}{\mathbf{D}_{\mathbf{orb}}}\ \mathbf{P}_{\mathbf{orb}} \tag{3.19}$$

where $\mathbf{P}_{\mathbf{orb}}$ contains all the polynomial coefficients of relative orbital errors with respect to the reference image and $\mathbf{D}_{\mathbf{orb}}$ is the design matrix relating the observations and the orbit error parameters. The phase differences at the arcs in all the interferograms due to topographic errors and deformation rates can be expressed as:

$$\underset{(M\times G)\times 1}{\Delta\Phi_{\mathbf{topo+defo}}} = \underset{(M\times G)\times(2\times(P-1))}{\mathbf{D}_{\mathbf{par}}}\ \underset{(2\times(P-1)\times 1)}{\mathbf{P}_{\mathbf{par}}} \tag{3.20}$$

where $\mathbf{P}_{\mathbf{par}}$ contains the deformation rate and DEM error at each coherent point except for one reference point. The final observation equation reflecting the relationship between the phase differences at the arcs and the unknowns (i.e., orbital error polynomial coefficients, topographic errors, and deformation rates) can be expressed as:

$$\underset{(M\times G)\times 1}{\Delta\Phi} = \mathbf{DP} + \underset{(M\times G)\times 1}{\mathbf{W}} \tag{3.21}$$

with

$$\begin{aligned} \mathbf{D} &= \left[\mathbf{D}_{\mathbf{orb}} \quad \mathbf{D}_{\mathbf{par}}\right]^T \\ \mathbf{P} &= \left[\mathbf{P}_{\mathbf{orb}} \quad \mathbf{P}_{\mathbf{par}}\right]^T \end{aligned} \tag{3.22}$$

where $\mathbf{W}$ is a vector that contains all the unmodeled phase at the arcs due to, e.g., spatially uncorrelated atmospheric delays and decorrelation noise. The parameters can be resolved by sparse least squares methods with a phase ambiguity detector (Zhang et al. 2012, 2013).

3.5 Parameter Estimation

3.5.1 Average Deformation Rate and DEM Error

After the topographic contribution from each interferogram is removed using an existing DEM, the phase value ϕ_i^k for the ith coherent point in the kth interferogram with a time separation of t^k can be expressed as:

$$\phi_i^k = c(v_i t^k + \mu_i^k) + \frac{cB_\perp^k h_i}{R^k \sin\theta^k} + \alpha_i^k + N \cdot 2\pi + n_i^k \tag{3.23}$$

where c is a constant equal to $(-4\pi/\lambda)$ and λ is the SAR wavelength. The first term on the right side represents ground surface deformation during the time period t^k and consists of two components: one due to constant velocity (v_i), and the other due to non-linear motion μ_i^k. The second term on the right side of the equation represents the phase component due to DEM error (h_i) and is related to: (1) the perpendicular baseline ($B_\perp^k$), which can be calculated using precision restitute vectors for ERS sensors (Massmann 1995; Scharroo et al. 1998), (2) the distance from the master sensor to the scene center (R^k), and (3) the SAR look angle (θ^k) at the scene center. The last term on the right side of Eq. 3.23, α_i^k, is the phase contribution due to atmospheric anomalies, and n_i^k represents the phase noise. Considering a set of differential interferograms, the observation model of MTInSAR has the following generalized form:

$$\mathbf{\Phi} = \mathbf{AP} + \mathbf{W} \tag{3.24}$$

where $\mathbf{\Phi}$ represents the input phases (which could be wrapped phases at arcs or unwrapped phases at points), $\mathbf{P}$ is an unknown vector whose elements could be h, v, and N, and $\mathbf{W}$ represents the remaining terms (i.e., the phase contributed by non-linear motion, atmospheric artifacts, and noise).

Differences among the various MTInSAR techniques described above are shown in Table 3.1. Based on a

Table 3.1 Comparison of MTInSAR techniques

MTInSAR techniques	Observation (Φ)		Parameter solved (P)	Type of interf.	Parameter solver
	Wrapped/Unwrapped	Point/Arc			
SBAS	Unwrapped	Point	h, $\bar{v}$	Multi-master	3.5.1.1
PSI	Wrapped	Arc	Δh, $\Delta\bar{v}$	Single-master	3.5.1.2
CPT	Wrapped	Arc	Δh, $\Delta\bar{v}$	Multi-master	3.5.1.2
STUN	Wrapped	Arc	Δh, $\Delta\bar{v}$, N	Single-master	3.5.1.3
TCPInSAR	Wrapped	Arc	Δh, $\Delta\bar{v}$	Multi-master	3.5.1.4

generalized model, we now introduce four methods used for parameter estimation.

3.5.1.1 Least Squares

When the observations are the unwrapped phases at the ith coherent point and the parameters are the mean deformation rate (v) and DEM error (h), Eq. 3.23 can be rewritten as

$$\mathbf{\Phi}_{i}^{unwrapped} = \mathbf{A}_i \begin{bmatrix} h \\ v \end{bmatrix} + \mathbf{W}_i \tag{3.25}$$

This is the basic model adopted by SBAS. The parameters can be retrieved by a least squares approach:

$$\begin{bmatrix} \hat{h} \\ \hat{v} \end{bmatrix} = (\mathbf{A}^{\mathbf{T}}\mathbf{A})^{-1}\mathbf{A}^{\mathbf{T}}\mathbf{\Phi}_{\mathbf{i}}^{\mathbf{unwrapped}} \tag{3.26}$$

It should be noted that although there are two resolved parameters, in SBAS only the DEM error term (h) is used for subsequent image processing.

3.5.1.2 Two-Dimensional Solution Search

When the observations are the wrapped phase differences at arcs constructed by point x and point y, and the parameters are the velocity difference ($\Delta v_{x,y}$) and height error difference ($\Delta h_{x,y}$), Eq. 3.23 can be rewritten as

$$\mathbf{\Phi}_{x,y}^{wrapped} = \mathbf{A}_{x,y} \begin{bmatrix} \Delta h_{x,y} \\ \Delta v_{x,y} \end{bmatrix} + \mathbf{W}_{x,y} \tag{3.27}$$

Since $\mathbf{\Phi}_{x,y}^{wrapped}$is ambiguous, the parameter estimation from Eq. 3.27 is a non-linear inversion problem. A temporal coherence index ($\gamma_{x,y}$) is commonly used for this inversion (Ferretti et al. 2001; Mora et al. 2003; Zhang et al. 2009). Given a total of M interferograms, $\gamma_{x,y}$ is defined as:

$$\gamma_{x,y} = \frac{1}{M}\left|\sum_{k=1}^{M} e^{-j\mathbf{W}_{x,y}^{k}}\right| \tag{3.28}$$

where $j = \sqrt{-1}$. By setting appropriate variation ranges for the velocity difference ($\Delta v_{x,y}$) and height error difference ($\Delta h_{x,y}$), one can search for the maximum coherence, $\gamma_{x,y}$, within the specified two-dimensional ranges using small sampling intervals. Then the values for $\Delta v_{x,y}$ and $\Delta h_{x,y}$ can be found. When $\Delta v_{x,y}$ and $\Delta h_{x,y}$ for all neighboring pixel sets are determined, the absolute values of DEM error and linear deformation rate at each coherent pixel can be derived through spatial integration with respect to an arbitrary reference point, where the DEM error and linear deformation rate are known or assumed to be zero. Note that the solution search can only be successfully performed under the condition of $\left|\omega_{i,x,y}^{k}\right| < \pi$, which can be met in most cases.

3.5.1.3 Integer Least Squares

When the observations are the wrapped phase differences at arcs constructed by point x and point y, and the parameters are velocity difference ($\Delta v_{x,y}$), height error difference ($\Delta h_{x,y}$) and integer ambiguities (N) in a total of M interferograms, Eq. 3.23 can be rewritten as (Kampes 2006):

$$\mathbf{\Phi}_{x,y}^{wrapped} = \begin{bmatrix} -2\pi & & & \\ & -2\pi & & \\ & & \ddots & \\ & & & -2\pi \end{bmatrix} \begin{bmatrix} N^1 \\ N^2 \\ \vdots \\ N^M \end{bmatrix} + \mathbf{A}_{x,y} \begin{bmatrix} \Delta h_{x,y} \\ \Delta v_{x,y} \end{bmatrix} + \mathbf{W}_{x,y} \tag{3.29}$$

For each arc, M integer ambiguities and 2 real-valued parameters have to be estimated from M observed wrapped phase differences. The solution to this system can only be obtained by using a priori knowledge of the integer nature of the ambiguities.

3.5.1.4 Least Squares with Phase Ambiguity Detector

For the system of observation equations shown in Eq. 3.27, the parameters cannot be estimated by linear inversion due to the existence of integer ambiguities. Although temporal coherence maximization has the ability to resolve average deformation rates and DEM errors from wrapped phase data, a parameter search by non-linear inversion might

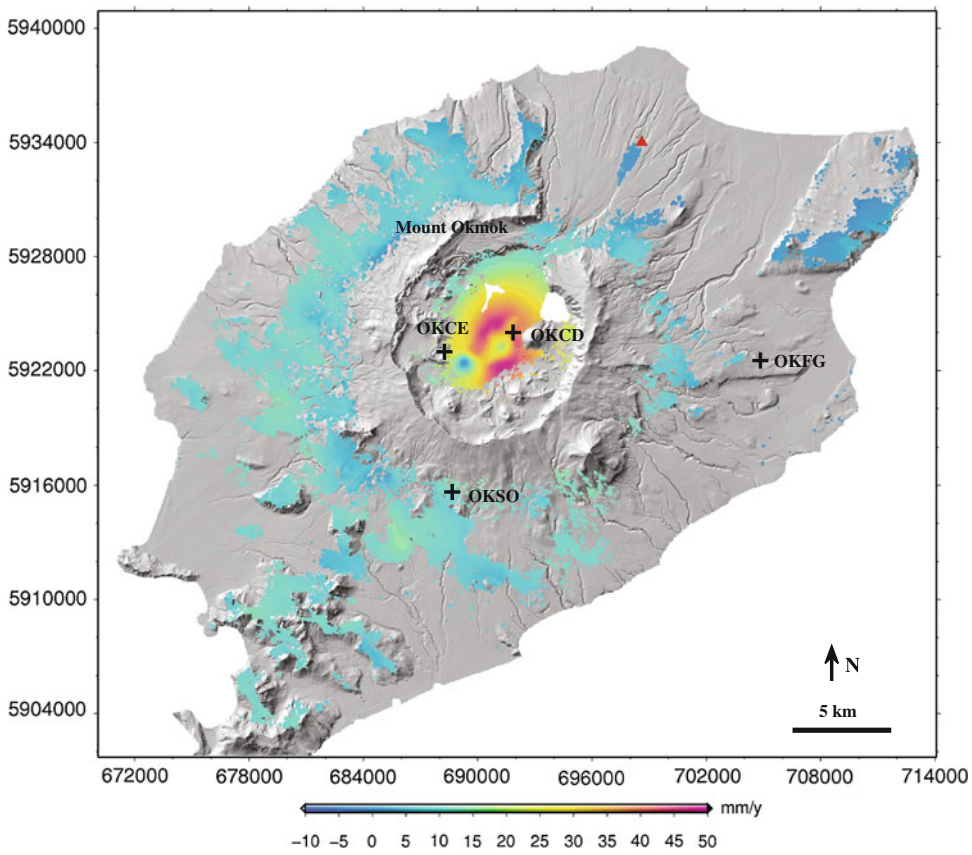

Fig. 3.1 Linear deformation rate at Mount Okmok based on PSInSAR processing of 19 Envisat SAR images during June 10, 2003 and July 8, 2008. *Red triangle* represents reference point for PSInSAR processing. *Crosses* represent CGPS stations

identify several local maxima (as is the case for any non-linear inversion problem). In this case, more than one choice of $\Delta v_{x,y}$ and $\Delta h_{x,y}$ might satisfy the observation equations, so a unique solution cannot be guaranteed. However, for an MTInSAR system in which multi-master interferograms with short baselines (spatial and temporal) are involved, there are usually sufficient arcs constructed by neighboring coherent pixels that do not have phase ambiguities. If these arcs can be reliably identified, parameter estimation on these arcs can be greatly simplified. For any arc regardless of phase ambiguities, the least squares solution of unknowns from Eq. 3.27 is as follows:

$$\begin{bmatrix} \Delta\hat{v} \\ \Delta\hat{h}_{x,y} \end{bmatrix} = (\mathbf{A}^{\mathbf{T}}\mathbf{P}_{\mathbf{x},\mathbf{y}}\mathbf{A})^{-1}(\mathbf{A}^{\mathbf{T}}\mathbf{P}_{\mathbf{x},\mathbf{y}}\Delta\Phi)$$
$$R = \Delta\Phi - (\mathbf{A}^{\mathbf{T}}\mathbf{P}_{\mathbf{x},\mathbf{y}}\mathbf{A})^{-1}(\mathbf{A}^{\mathbf{T}}\mathbf{P}_{\mathbf{x},\mathbf{y}}\Delta\Phi) \quad (3.30)$$

where R is the least squares residual vector and $P_{x,y}$ is the weight matrix, which can be obtained by taking the inverse of a prior variance matrix of the double-difference phases (Zhang et al. 2011b). Experience shows that the least squares residuals for an arc with and without phase ambiguities are quite different, indicating that phase ambiguities can bias the parameter estimation significantly (Zhang et al. 2011b, 2012). Therefore, an ambiguity detector can be designed by taking account of the least squares residuals. Details of this method can be found in Zhang et al. (2011b, 2012, 2013). After removing the arcs with phase ambiguities, parameters for the remaining arcs are integrated to obtain parameter estimates at all coherent points with respect to a designated reference point.

3.5.2 Deformation Time Series

After the average deformation rate and DEM errors have been resolved (Sect. 3.5.1) and the phase contributions due to atmospheric path-delay anomalies have been removed (Sect. 3.3), it is possible to retrieve the non-linear deformation component and then build up a full resolution deformation time series. The basic observation function for non-linear rate estimation can be written as:

$$\mathbf{\Phi}_{\mathbf{res}} = \mathbf{B}\mathbf{V}_{\mathbf{nonlinear}} + \mathbf{W}_{\mathbf{res}} \quad (3.31)$$

where $\mathbf{\Phi}_{\mathbf{res}}$ is the phase residual vector, $\mathbf{B}$ is the design matrix showing the relationship between non-linear deformation rates and phase residuals, $\mathbf{V}_{\mathbf{nonlinear}}$ is the non-linear rate vector, and $\mathbf{W}_{\mathbf{res}}$ is the noise vector in the phase residual. The non-linear rates can be resolved by least squares, as explained

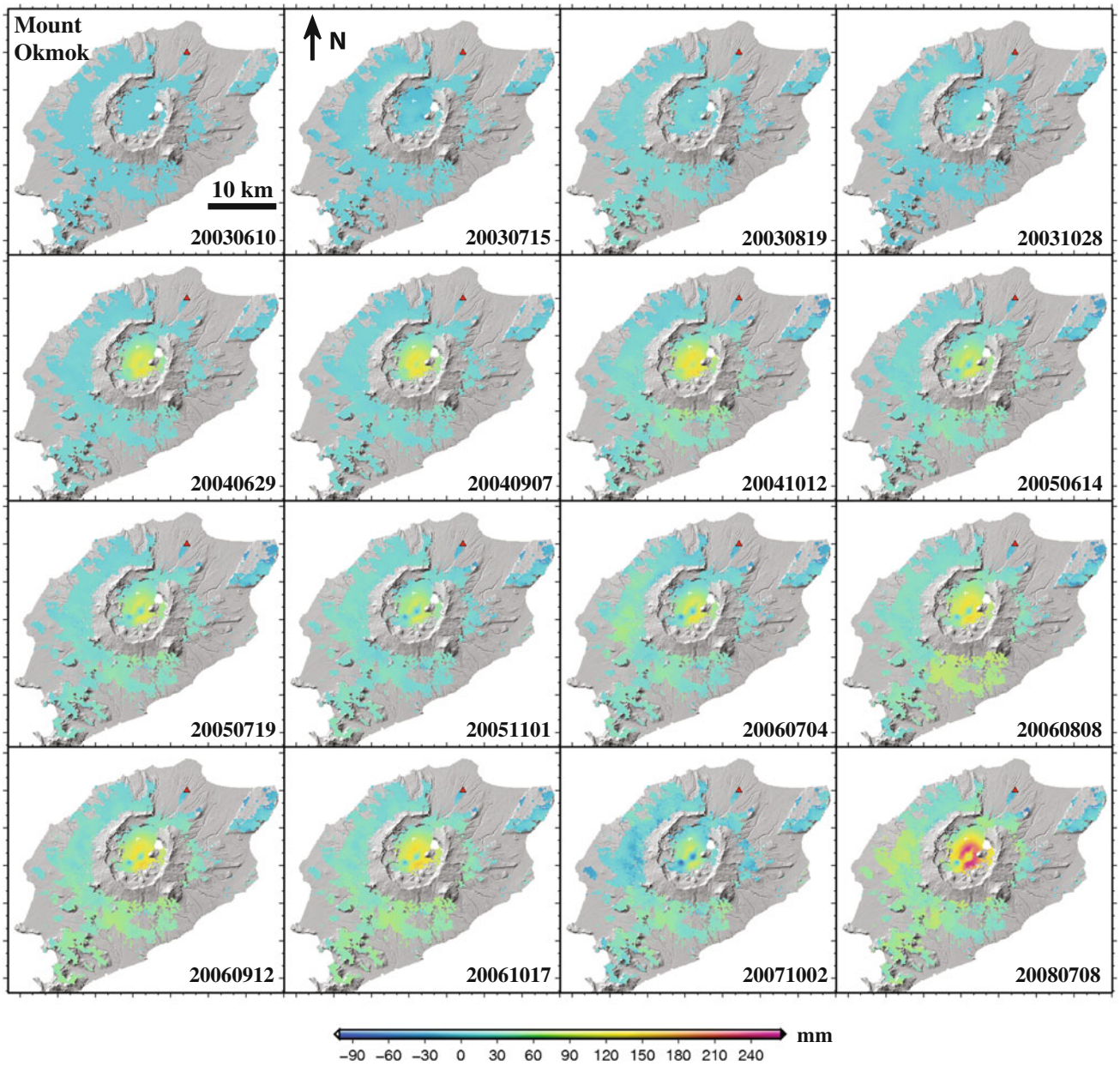

Fig. 3.2 Time-series PSInSAR deformation maps for Mount Okmok for 2003–2008. Image in *lower right corner* is for July 8, 2008, five days before the July 12, 2008 eruption

above (Zhang et al. 2012, 2013). When the design matrix **B** exhibits rank deficiency, its pseudoinverse is employed to get the minimum norm least squares solution. The final full-resolution deformation time series then can be obtained by combining the linear deformation rates (**v**) and non-linear deformation rates ($\mathbf{V}_{\mathbf{nonlinear}}$).

Figure 3.1 shows the distribution of PSs on Mount Okmok, as identified from a stack of 19 Envisat SAR images (see Chap. 6, Okmok section). Based on our experience, the image represents a typical coherence map for a C-band InSAR image of Okmok. The average inflation rate during 2003–2008 from PSInSAR processing is slightly less than 50 mm/year. Subsidence of 1997 lava flows on parts of the caldera floor also is discernible.

Figure 3.2 shows time-series deformation maps for the period 2003–2008 at Okmok, and Fig. 3.3 compares displacement time series derived from PSInSAR with measurements at the same four sites from CGPS. The time series are complementary and they match reasonably well where they overlap in time (i.e., mostly within one standard

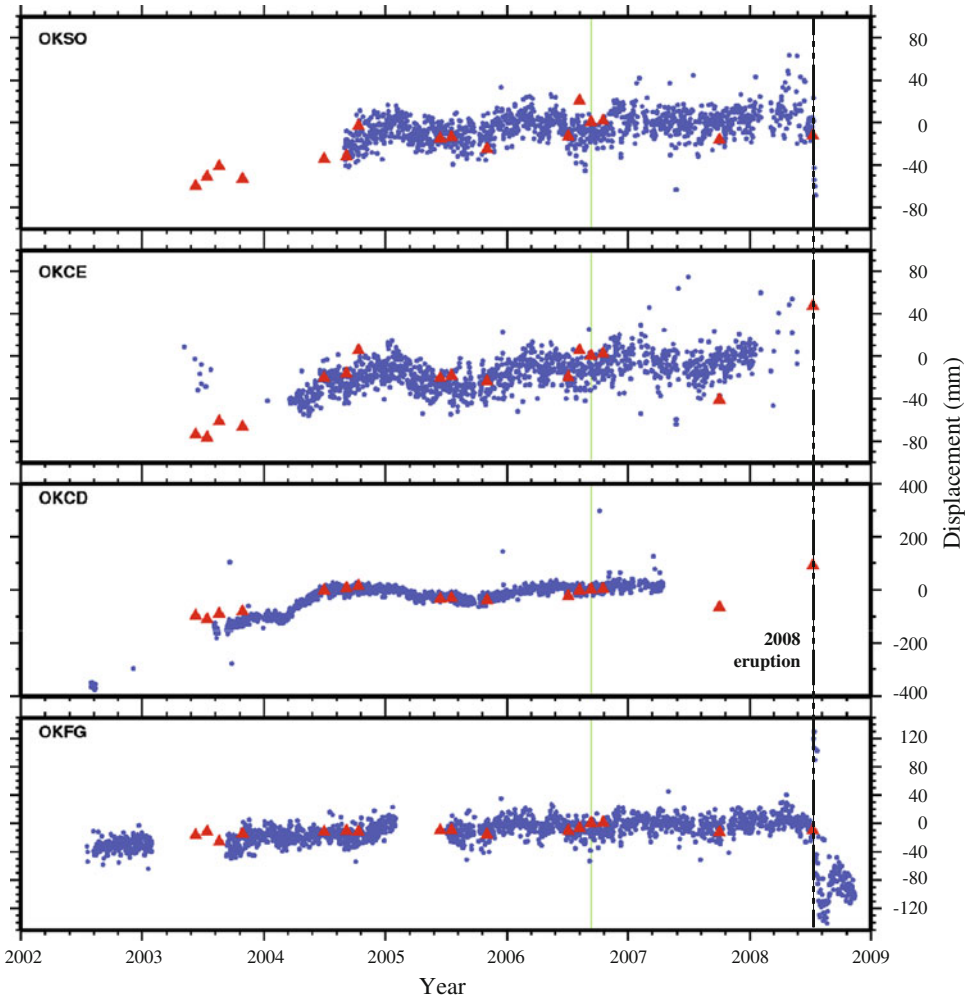

Fig. 3.3 Comparison of time-series PSInSAR measurements (*red triangles*) with CGPS observations (*blue dots*) at Mount Okmok. PSInSAR time series are with respect to the reference pixel on the northern flank of Okmok (*red triangle* in Fig. 3.1) and the start time of June 10, 2003. Locations of CGPS sites are shown in Fig. 3.1. Data gaps exist in CGPS measurements

deviation in the CGPS measurements), which demonstrates that MTInSAR can be useful either as a stand-alone tool or in conjunction with other deformation monitoring techniques.

3.6 Summary of Current MTInSAR Techniques

3.6.1 PSInSAR

PSInSAR has the following advantages compared to conventional InSAR techniques:

- With the PSInSAR technique, all available SAR images can be exploited without much concern for the baseline separations. For conventional InSAR, only relatively short baselines can be used for deformation analysis to avoid coherence loss. This limitation generally results in a substantial loss of temporal coverage.
- With PSInSAR, atmospheric artifacts can be mostly removed, eliminating a serious limitation of conventional InSAR in cases where real ground deformation is small and smoothly varying across the scene.
- With PSInSAR, single coherent pixels can be identified. This feature is essential in the case of large temporal and geometric baselines, where only pointwise targets carry useful phase information. No useful information can be extracted by conventional InSAR techniques under these conditions.
- With PSInSAR, terrain heights at PS pixels can be improved significantly to an accuracy which is unattainable by conventional InSAR techniques.

On the other hand, PSInSAR is a sophisticated multi-spatial and multi-temporal InSAR processing method that requires more than $\sim$30 InSAR images of the study area to complete an analysis—a significant disadvantage for targets with limited SAR coverage. Therefore, PSInSAR is not intended to replace the conventional InSAR approach. Rather, this novel technique has great potential to enhance the capability for surface deformation monitoring in areas for which adequate SAR coverage is available and where the deformation rate is too small to be measured reliably with conventional InSAR methods.

3.6.2 Small Baseline Subset (SBAS) InSAR

The SBAS InSAR algorithm was first demonstrated by Berardino et al. (2002) as a means to mitigate atmospheric artifacts and topographic errors in time-sequential interferograms, and thus to obtain time-series deformation information. The algorithm uses only interferograms with small baselines that overlap in time in order to reduce spatial decorrelation. To extract deformation time-series information from multiple-temporal interferograms, the SBAS algorithm estimates the mean deformation rate and the topographic error using unwrapped interferograms. Atmospheric artifacts are mitigated through temporal high-pass and spatial low-pass filtering of the interferograms after the mean deformation rates have been removed. Because the interferograms are not adjacent in time (i.e., there may be temporal overlap or underlap between them), SBAS InSAR uses the singular value decomposition (SVD) approach based on a minimum-norm criterion of the deformation rate to derive time-series deformation estimates.

Various enhancements of the original SBAS algorithm have been developed in order to: (1) suppress errors caused by temporal decorrelation and other noise effects, (2) improve the linear deformation rate estimate by avoiding phase unwrapping errors, (3) improve estimates of atmospheric artifacts and topographic errors, and (4) address the atmospheric artifact and orbital error at a specific reference point (a pixel location used to reference interferogram phase values at other pixels). For example, Lee et al. (2010) implemented a refined SBAS InSAR algorithm that improves estimates of time-series deformation in four respects. First, phase unwrapping errors are corrected by distinguishing between high-quality InSAR images in which no unwrapping errors could be found and low-quality ones where phase jumps due to unwrapping errors are likely. The mean deformation rates at all coherent pixel locations are estimated from the high-quality interferograms. New, wrapped residual interferograms are formed by subtracting the estimated linear deformation rate from each interferogram on a pixel-by-pixel basis. The residual interferograms are then unwrapped to create new unwrapped interferograms. This step essentially removes phase unwrapping errors from the low-quality interferograms, because the fringe rates in the residual interferograms are much lower than those in the original interferograms. Second, the temporal noise is mitigated further by the finite difference smoothing approach (Schmidt and Bürgmann 2003). Time-series deformation histories are estimated at each coherent pixel using the SVD operation and are removed from each of the interferograms. Atmospheric artifacts in the residual interferograms are then removed by temporal high-pass and spatial low-pass filtering operations (recall that atmospheric artifacts generally are spatially correlated and temporally random). After the atmospheric contributions are removed in this way, the deformation time series is recomputed by simultaneously applying the SVD approach and the finite difference smoothing method (Schmidt and Bürgmann 2003) in order to further suppress the noise contribution. Third, procedures are implemented to correct any possible phase bias at the reference point due to orbital and atmospheric phase artifacts (e.g., Lee et al. 2010). Finally, estimates of atmospheric artifacts, topographic errors, and time-series deformation measurements are refined through an iteration procedure. Examples of SBAS processing for Augustine and Seguam volcanoes are included in Chap. 6 of this report.

3.6.3 Combined PSInSAR and SBAS Processing

In the original PSInSAR method, a single image is designated as the master (reference) and the phase differences between the master image and all associated slave images are used as the basic observation to estimate the average deformation rate and topography error. The SBAS InSAR method differs in that SBAS InSAR uses all suitable small-baseline interferograms (i.e., multiple masters) to minimize the effects of coherence loss and topography error. Traditional PSInSAR identifies individual PSs based on the stability (and/or coherence) of the phase signal over time, whereas SBAS InSAR locates coherent patches based on the coherence of interferograms in the spatial domain. Prefiltering or multi-looking is not applied in PSInSAR processing prior to interferogram generation in order to ensure that PS signatures are undistorted. SBAS processing, on the other hand, typically is applied to multi-looked (and filtered) interferograms. A useful hybrid approach combines PSInSAR and SBAS concepts by conducting time-series InSAR analysis using interferograms based on multiple masters (e.g., Mora et al. 2003; Hooper and Zebker 2007; Hooper 2008; Zhang et al. 2011b, 2012). PS or temporally coherent pixels are selected using one or more PS identification procedures. Interferometric phases at PSs, either wrapped (Zhang et al. 2011b, 2012) or unwrapped by way of a 3-D phase unwrapping procedure (Hooper and Zebker 2007), are analyzed with SBAS processing at full resolution using least-squares (Schmidt and Bürgmann 2003), singular value decomposition (Berardino et al. 2002), or L1-norm minimization (Lauknes et al. 2011; Zhang et al. 2013). Atmospheric correction is done using procedures described in Sect. 3.3. The final result is a deformation time series for each PS, which can be combined to produce a series of deformation maps as a function of time if the density of PSs is sufficient.

References

Adam, N., Kampes, B., & Eineder, M. (2004). Development of a scientific permanent scatterer system: Modifications for mixed ERS/ENVISAT time series. In *ENVISAT & ERS Symposium.* Salzburg, Astria, September 6–10, 2004 (pp. 1–9) (CD-ROM).

Bamler, R. (2000). Principles of synthetic aperture radar. *Surveys in Geophysics, 21*(2–3), 147–157. doi:10.1023/A:1006790026612.

Berardino, P., Fornaro, G., Fusco, A., Galluzzo, D., Lanari, R., Sansosti, E. et al. (2001). A new approach for analyzing the temporal evolution of earth surface deformations based on the combination of DIFSAR interferograms. In *Proceedings of 2001 International Geoscience and Remote Sensing Symposium (IGARSS'01).* Sydney, Australia.

Berardino, P., Fornaro, G., Lanari, R., & Sansosti, E. (2002). A new algorithm for surface deformation monitoring based on small baseline differential SAR interferograms. *IEEE Transactions on Geoscience and Remote Sensing, 40*, 2375–2383.

Biggs, J., Wright, T., Lu, Z., & Parsons, B. (2007). Multi-interferogram method for measuring interseismic deformation: Denali fault, Alaska. *Geophysical Journal International, 170*, 1165–1179. doi: 10.1111/j.1365-246X.2007.03415.x.

Blanco, P., Mallorquí, J. J., Duque, S., & Monells, D. (2008). The coherent pixels technique (CPT): An advanced DInSAR technique for non-linear deformation monitoring. *Pure and Applied Geophysics, 165*, 1167–1193.

Ferretti, A., Prati, C., & Rocca, F. (2000). Nonlinear subsidence rate estimation using permanent scatterers in differential SAR interferometry. *IEEE Transactions on Geoscience and Remote Sensing, 38*, 2202–2212.

Ferretti, A., Prati, C., & Rocca, F. (2001). Permanent scatterers in SAR interferometry. *IEEE Transactions on Geoscience and Remote Sensing, 39*, 8–20.

Ferretti, A., Fumagalli, A., Novali, F., Prati, C., Rocca, F., & Rucci, A. (2011). A new algorithm for processing interferometric data-stacks: SqueeSAR. *IEEE Transactions on Geoscience and Remote Sensing, 49*, 3460–3470.

Hanssen, R. (2001). *Radar interferometry: Data interpretation and error analysis* (p. 328). Dordrecht, The Netherlands: Kluwer Academic Publishers.

Hooper, A. (2008). A multi-temporal InSAR method incorporating both persistent scatterer and small baseline approaches. *Geophysical Research Letters, 35*, L16302. doi:10.1029/2008GL034654.

Hooper, A., & Zebker, H. (2007). Phase unwrapping in three dimensions with application to InSAR time series. *Journal of the Optical Society of America A-Optics Image Science and Vision*, *24*, 2737–2747.

Hooper, A., Zebker, H., Segall, P., & Kampes, B. (2004). A new method for measuring deformation on volcanoes and other natural terrains using InSAR persistent scatterers. *Geophysical Research Letters, 31*, L23611. doi:10.1029/2004GL021737.

Hooper, A., Bekaert, D., Spaans, K., & Arıkan, M. (2012). Recent advances in SAR interferometry time series analysis for measuring crustal deformation. *Tectonophysics, 514–517*, 1–13.

Kampes, B. M. (2006). *Radar interferometry: Persistent scatterer technique* (p. 227). Dordrecht: Springer.

Lanari, R., Mora, O., Manunta, M., Mallorqui, J. J., Berardino, P., & Sansosti, E. (2004). A small-baseline approach for investigating deformations on full-resolution differential SAR interferograms. *IEEE Transactions on Geoscience and Remote Sensing, 42*, 1377–1386.

Lauknes, T. R., Zebker, H. A., & Larsen, Y. (2011). InSAR deformation time series using an L1-norm small-baseline approach. *IEEE Transactions on Geoscience and Remote Sensing, 49*(1), 536–546.

Lee, C.-W., Lu, Z., Jung, H.-S., Won, J.-S., Dzurisin, D. (2010) Surface deformation of Augustine Volcano, 1992–2005, from multiple-interferogram processing using a refined small baseline subset (SBAS) interferometric synthetic aperture radar (InSAR) approach, Chapter 18. In J. Power, M. L. Coombs, & J. T. Freymueller (Eds.), *The 2006 Eruption of Augustine Volcano* (pp. 453–465). Alaska: U.S. Geological Survey Professional Paper 1769, available at http://pubs.usgs.gov/pp/1769/chapters/p1769_chapter18.pdf

Lin, Y. N., Simons, M., Hetland, E. A., Muse, P., & DiCaprio, C. (2010). A multiscale approach to estimating topographically correlated propagation delays in radar interferograms: Geochemistry. *Geophysics and Geosystems (G3), 11*, Q09002. doi: 10.1029/2010GC003228.

Liu, S. Z. (2012). Satellite radar interferometry: estimation of atmospheric delay. Ph.D. Thesis, Delft University of Technology.

Massmann, F. H. (1995). Information for ERS PRL/PRC Users. Technical note, GeoForschungsZentrum (German Processing and Archiving Facility (D-PAF)), Potsdam.

Mora, O., Mallorquí, J. J., & Broquetas, A. (2003). Linear and nonlinear terrain deformation maps from a reduced set of interferometric SAR images. *IEEE Transactions on Geoscience and Remote Sensing, 41*, 2243–2253.

Sandwell, D. T., & Price, E. J. (1998). Phase gradient approach to stacking interferograms. *Journal of Geophysical Research, 103*, 30183–30204.

Scharroo, R., Visser, P., & Mets, G. (1998). Precise orbit determination and gravity field improvement for ERS satellites. *Journal of Geophysical Research, 103*, 8113–8127.

Schmidt, D., & Bürgmann, R. (2003). Time-dependent land uplift and subsidence in the Santa Clara valley, California, from a large interferometric synthetic aperture radar data set. *Journal of Geophysical Research, 108*(B9), 2416. doi:10.1029/2002JB002267.

Shanker, P., & Zebker, H. (2007). Persistent scatterer selection using maximum likelihood estimation. *Geophysical Research Letters, 34*(22), 2–5. doi:10.1029/2007GL030806.

Shirzaei, M., & Bürgmann, R. (2012). Topography correlated atmospheric delay correction in radar interferometry using wavelet transforms. *Geophysical Research Letters, 39*, L01305. doi: 10.1029/2011GL049971.

Werner, C., Wegmuller, U., Strozzi, T., & Wiesmann, A. (2003). Interferometric point target analysis for deformation mapping. In *IEEE Proceedings, International Geoscience and Remote Sensing Symposium.* Toulouse, France, July 21–25, 2003 (pp. 4362–4364).

Williams, S., Bock, Y., & Pang, P. (1998). Integrated satellite radar interferometry: Tropospheric noise, GPS estimates and implications for interferometric synthetic aperture radar products. *Journal of Geophysical Research, 103*, 27051–27067.

Zebker, H., Rosen, P., & Hensley, S. (1997). Atmospheric effects in interferometric synthetic aperture radar surface deformation and topographic maps. *Journal of Geophysical Research, 102*, 7547–7563.

Zhang, Y., Zhang, J., Gong, W., & Lu, Z. (2009). Monitoring urban subsidence based on SAR interferometric point target analysis. *Acta Geodaetica et Cartographica Sinica, 38*(6), 482–487, 493.

Zhang, L., Ding, X. L., & Lu, Z. (2011a). Ground settlement monitoring based on temporarily coherent points between two SAR acquisitions. *ISPRS Journal of Photogrammetry and Remote Sensing, 66*(1), 146–152.

Zhang, L., Ding, X. L., & Lu, Z. (2011b). Modeling PSInSAR time-series without phase unwrapping. *IEEE Transactions on Geoscience and Remote Sensing, 49*(1), 547–556. doi: 10.1109/TGRS.2010.2052625.

Zhang, L., Lu, Z., Ding, X. L., Jung, H. S., Feng, G. C., & Lee, C. W. (2012). Mapping ground surface deformation using temporarily

coherent point SAR interferometry: Application to Los Angeles Basin. *Remote Sensing of Environment, 117*, 429–439.

Zhang, L., Ding, X. L., Lu, Z., Jung, H. S., & Feng, G. C. (2013). A novel multi-temporal InSAR model for joint estimation of deformation rates and orbital Errors. *IEEE Transactions on Geoscience and Remote Sensing* (in press), doi: 10.1109/TGRS.2013.2273374